Influence of water fugacity and activation volume on the flow properties of fine-grained anorthite aggregates

E. Rybacki,[1] M. Gottschalk,[1] R. Wirth,[1] and G. Dresen[1]

Received 1 February 2005; revised 16 November 2005; accepted 27 December 2005; published 30 March 2006.

[1] To specify quantitatively the effect of pressure and water weakening on the flow strength of feldspar we performed triaxial creep experiments in a gas deformation apparatus at temperatures of 1000–1150°C, confining pressures of 100–450 MPa, and axial stresses of 10–400 MPa, resulting in strain rates of $\sim 6 \times 10^{-7}$ to 3×10^{-3} s^{-1}. Dense samples with a grain size of ~ 3 μm were prepared by hot-isostatic pressing of anorthite glass powder. Hydrous samples contain about 0.33 ± 0.14 wt % H_2O and dry specimens 0.0005–0.02 wt % H_2O. The estimated residual glass content of wet samples is <2 vol %. Samples deformed by grain boundary diffusion-controlled creep at low stresses and dislocation creep at stresses ≳150 MPa. We estimate an activation volume of $V \approx 24$ $cm^3 mol^{-1}$ for anhydrous samples deforming in diffusion creep. For wet samples, deformed in hydrous conditions with varying buffers fixing oxygen fugacity, the activation volume is about 38 cm^3 mol^{-1}. Creep rate of hydrous anorthite aggregates depends on water fugacity raised to a power of $r = 1.0 \pm 0.3$, suggesting hydrolysis of oxygen bonds. Considering the effect of activation volume and water fugacity on extrapolation of constitutive laws to conditions prevailing in the continental lower crust, viscosities of hydrous feldspar aggregates increase by a factor of <3.

Citation: Rybacki, E., M. Gottschalk, R. Wirth, and G. Dresen (2006), Influence of water fugacity and activation volume on the flow properties of fine-grained anorthite aggregates, *J. Geophys. Res.*, *111*, B03203, doi:10.1029/2005JB003663.

1. Introduction

[2] Quantitative estimates of the viscosity of the Earth's lower crust and upper mantle are based on modeling of postseismic surface deformation [*Freed and Burgmann*, 2004; *Hetland and Hager*, 2003; *Hu et al.*, 2004; *Kenner*, 2004; *Nishimura and Thatcher*, 2003; *Vergnolle et al.*, 2003] and extrapolation of laboratory measurements to natural conditions [e.g., *Kohlstedt et al.*, 1995; *Montesi and Hirth*, 2003]. Early experimental investigations on natural samples revealed that so-called "dry" or anhydrous rocks are much stronger than "wet" or hydrous aggregates, see reviews by *Evans and Dresen* [1991] and *Evans and Kohlstedt* [1995]. The terms "dry" and "wet" indicate mainly the heat treatment of samples before deformation, e.g., water-added, as-is or untreated, oven-dried, or vacuum-dried, but usually without specification of water content or the type of hydrogen incorporation, e.g., as fluid inclusions or structurally bonded hydrogen.

[3] Almost 40 years ago, *Griggs and Blacic* [1965] and *Griggs* [1967] in their pioneering studies observed that flow strength of quartz decreases significantly in the presence of trace amounts of water, which they attributed to hydrolysis of O-Si-O bonds. Hydrolytic weakening was subsequently observed in a plethora of experimental studies on quartz [*Hobbs et al.*, 1972; *Koch et al.*, 1989; *Kronenberg et al.*, 1986; *Kronenberg and Tullis*, 1984; *Ord and Hobbs*, 1986; *Post et al.*, 1996], although the physics of the process and solid state reactions involved still remain enigmatic [*Paterson*, 1989]. A significant reduction of high-temperature flow strength has been discovered for the dominant mineral constituents of the crust and upper mantle such as feldspar [*Dimanov et al.*, 1999; *Rybacki and Dresen*, 2000, 2004; *Tullis and Yund*, 1980; *Tullis et al.*, 1996], pyroxene [*Hier-Majumder et al.*, 2005; *McDonnell*, 1998; *McDonnell et al.*, 2000; *Mei et al.*, 2001], and olivine [*Chopra and Paterson*, 1984; *Karato et al.*, 1986; *Karato and Jung*, 2003; *Mei and Kohlstedt*, 2000a, 2000b].

[4] Concentration of water-related point defects in rocks depends on thermodynamic conditions if transport kinetics are fast enough to allow for equilibration. For water-saturated rocks in thermodynamic equilibrium, solubility of water-related defects in silicates and high-temperature creep rate $\dot{\varepsilon}$ were found to increase with water fugacity f_{H_2O} raised to the power of r, i.e., $\dot{\varepsilon} \propto f_{H_2O}^r$ [*Karato et al.*, 1986; *Paterson*, 1989]. When rocks are undersaturated with respect to water or thermodynamic equilibrium was not achieved, the constitutive behavior may be differently affected by water content. For example, creep activation energy may depend on water concentration, or the rate-limiting creep mechanism may change with water content [*Rybacki and Dresen*, 2000].

[5] Estimates of the water fugacity exponent r for high-temperature creep of silicates are still scarce. For quartzite,

[1] GeoForschungsZentrum Potsdam, Potsdam, Germany.

0148-0227/06/2005JB003663$09.00

exponents r range between 1 and 2, suggesting the replacement of oxygen by OH^- or silicon by H^+, respectively [*Gleason and Tullis*, 1995; *Hirth et al.*, 2001; *Kohlstedt et al.*, 1995; *Post et al.*, 1996; *Rutter and Brodie*, 2004]. For creep of Fe-bearing olivine aggregates, *Mei and Kohlstedt* [2000a, 2000b] estimated a water fugacity exponent between 0.69 and 1.25 assuming activation volumes V of 0 and 38 cm^3mol^{-1}, respectively, and *Karato and Jung* [2003] obtained $r = 1.20$ with $V = 24$ cm^3mol^{-1}. *Hier-Majumder et al.* [2005] measured an exponent of 1.4 for diffusion creep of wet clinopyroxenite. For diffusion creep of hydrous feldspar aggregates the fugacity exponent was estimated $r \approx 0.5$ [*Rybacki and Dresen*, 2000]. In this study, we investigate the effect of water fugacity on the constitutive behavior of water-saturated synthetic anorthite aggregates. In this context, the creep activation volume was estimated from deformation experiments performed on dry and wet specimens.

2. Experimental Methods

2.1. Starting Material and Sample Preparation

[6] Synthetic specimens were fabricated from crushed $CaAl_2Si_2O_8$ glass powder with a particle size of either <11 μm or <60 μm (Schott Glaswerke, An_{99} composition). Initially, powders were cold pressed into iron cans of 0.5 mm wall thickness at an axial pressure of about 200 MPa in a vacuum chamber at about 1.5 kPa pressure. A few small anorthite single crystals (~2 mm in size) were added to the powder used to produce some wet specimens (Pl14–Pl17). The single crystals allowed estimating the amount of intracrystalline water incorporated at test conditions. Hot pressing was performed in a Paterson-type gas deformation apparatus at 300 MPa pressure. To enhance compaction, samples were kept initially at 877°C temperature for 0.5 hour, which is slightly above the glass transition temperature of 871°C [*Dresen et al.*, 1996]. To crystallize the glass, samples were subsequently annealed at 1100°C for 22 hours, exceeding the nucleation temperature by about 80°C [*Dresen et al.*, 1996]. After hot-pressing iron jackets were removed by dissolving in acid and cylindrical samples were precision ground to dimensions of 10 × 20 and 6.9 × 14 mm (diameter times length) for dry and wet samples, respectively. One hot-pressed sample (Pl06) was cut into parts of 10 × 10 mm in size. To produce dry samples hot-pressed aggregates were dried in an oven at 860–970°C for 260–480 hours duration. Final porosity of samples is less than about 0.5% as determined by Archimedes' method and submersion of samples in ethanol.

2.2. Water Content

[7] A Fourier-transformed infrared spectrometer (FTIR, Bruker IFS-66v) was used to measure the water content on ~150 μm thick doubly polished sections. Spectra were recorded at room temperature in the wave number range 2500 to 4000 cm^{-1}. The shape of measured spectra is generally broad without distinct peaks, representative of molecular water. Measurements performed on polycrystalline sections represent the bulk water content since the spot size of the spectrometer (minimum ~20 μm) spans several grains including grain boundaries. We calculated the water concentration from the peak height of absorbance spectra using Beer-Lambert's law with a molar extinction coefficient of 32 $L_{(H_2O)}$ mol^{-1} [*Beran*, 1987]. Reported values (Table 1) are about half as high compared to calculations using the integrated absorbance [*Johnson and Rossman*, 2003; *Libowitzky and Rossman*, 1997; *Paterson*, 1982].

[8] Undeformed wet samples contained 0.22 ± 0.08 wt % H_2O (33400 ± 12400 ppm H/Si) which is similar to the average water content measured for "typical" plutonic feldspars [*Johnson and Rossman*, 2004]. Measurements of the embedded (optically clear) single crystals yielded 0.04 ± 0.01 wt % H_2O (6800 ± 1700 ppm H/Si), which is about 4.5 times higher than their water content prior to hot-isostatic pressing (1500 ± 490 ppm H/Si). If equilibrated under experimental (hot press) conditions, this value may represent the intracrystalline water solubility. For comparison, *Johnson and Rossman* [2003] measured about 3100 ppm H/Si on natural anorthite crystals from tholeiitic origin. Since the bulk hydroxyl content is about 5 times higher than for single crystals most of the water is expected to be located on grain boundaries. The most significant difference between spectra of single crystals and polycrystalline feldspar is a shift of the absorbance peak from 3200–3400 cm^{-1} to slightly above 3500 cm^{-1}, probably indicating the presence of water-bearing melt inclusions on grain boundaries [*Johnson and Rossman*, 2004].

[9] The water content of dry samples was determined only after deformation. It is about 0.0025 ± 0.0005 wt % H_2O (380 ± 80 ppm H/Si) for specimens obtained from fine-grained powder (<11 μm, samples P106-1, P106-2, P123, P130, P131) and 0.020 ± 0.003 wt % H_2O (3100 ± 500 ppm H/Si) for anhydrous samples fabricated from coarse-grained glass powder (<60 μm, samples P107, P108, P124) (Table 1). Predrying of some powder batches, as well as drying of some cold-pressed aggregates at 850°C for several days under reducing atmosphere, has no influence on the final water content.

2.3. Microstructure

[10] Grain shape and size was analyzed by scanning electron microscopy (SEM, Zeiss DSM 962) of thermally etched sections. Grains are often prismatic and twinned. The average grain size was determined with the line intercept method [*Underwood*, 1970]. To correct for stereological truncation effects mean intercept lengths are multiplied by a factor of 1.9, assuming a grain aspect ratio of 2.5. The mean grain size is 2.7 ± 0.6 μm for deformed dry samples and 3.5 ± 0.4 μm for deformed wet samples, respectively. For some samples we estimated grain size before and after deformation and found no significant grain growth during testing. These observations agree with findings of [*Rybacki and Dresen*, 2000] on a similar starting material.

[11] Microstructures were investigated using a Philips CM200 transmission electron microscope (TEM). Samples with large electron-transparent areas were prepared using a focused iron beam instrument (Fei FIB200) [*Wirth*, 2004]. Dislocations are rarely found in the undeformed starting material irrespective of water content. Some grains contain finely spaced twins and antiphase domains that are likely due to phase transformations during crystallization and annealing of the starting anorthite glass [*Carpenter*, 1991]. In general, with increasing water content we observed fewer submicron-sized grains, less twins, and more antiphase

Table 1. Material Properties and Test Conditions of Synthetic Anorthite Aggregates

		Deformation Conditions		Deformed		Undeformed		
Sample[a]	T, °C	P, MPa	C_{H2O},[b] ppm H/Si	d, μm	C_{H2O},[b] ppm H/Si	d_{Powder}, μm	Jacketing	Comment
				Dry Samples				
Pl23	1125	400, 300, 200, 100	470	2.9 ± 0.4		<11 (predried)	Fe	extension
Pl30	1140	400, 300, 200, 100	410	3.5 ± 1.2		<11	Fe	extension
Pl07	1150	400, 300, 200, 100	3000	2.4 ± 0.4		<60	Fe	
Pl24	1160	400, 300,200, 100	3700	3.2 ± 0.8		<60	Fe	extension, second run
Pl06_1	1175	300, 200	250	1.9 ± 0.4		<11 (predried)	Fe	extension, preloaded
Pl06_2	1175	400	400	1.9 ± 0.3		<11 (predried)	Fe	
Pl31	1185	400, 300, 200	380	3.1 ± 0.9		<11	Fe	extension, much CO_2
Pl08	1200	400, 300, 200	2700	2.3 ± 0.3		<60	Fe	
				Wet Samples				
Pl13	1000	100	57000	3.9 ± 0.9	20100	<11 (predried)	Ni-Fe-Fe	second run
Pl25	1000	300	54300	4.0 ± 1.0		<11	Ni-Fe-Fe	
Pl21	1000	400	60100	3.3 ± 0.9	16300	<11 (predried)	Ni-Fe-Fe	
Pl19	1050	100			34600	<11 (predried)	Ni-Fe-Fe	fracture
Pl26	1050	300	33100	3.3 ± 0.8		<11	Ni-Fe-Fe	
Pl18	1050	400	63800	3.8 ± 0.7	32300	<11 (predried)	Ni-Fe-Fe	
Pl33	1050	450, 300, 150	77600	3.9 ± 1.0		<11	Fe-Fe-Fe	
Pl34	1050	450, 300, 150	60100	3.7 ± 0.8		<11	Fe-Fe-Fe	
Pl32	1050	450, 300	39600	3.8 ± 0.9		<11	Ni-Ni-Ni	second run, fracture
Pl35	1050	450, 300	12600	4.2 ± 1.0		<11	Ni-Ni-Ni	fracture
Pl36	1050	450, 300, 150	64500	3.8 ± 0.7		<11	Cu-Cu-Cu	
Pl37	1050	450, 300, 150	74800	3.7 ± 0.9		<11	Cu-Cu-Cu	
Pl17	1100	100	39500 ± 17100 (sc:5900 ± 700)	3.6 ± 1.1	59300	<11	Ni-Fe-Fe	second run embedded single crystals
Pl14	1100	200	21400 ± 14200 (sc:4400 ± 2300)	2.8 ± 0.7	43400 ± 17700 (sc:5100 ± 1100)	<11	Ni-Fe-Fe	embedded single crystals
Pl15	1100	300	29500 ± 18900 (sc:3300 ± 1400)	3.0 ± 0.4	28500 (sc:8500 ± 2200)	<11	Ni-Fe-Fe	embedded single crystals
Pl16	1100	400	35800 ± 15300 (sc:6300 ± 900)	3.2 ± 0.8	38500 ± 7200 (sc:6900 ± 2100)	<11	Ni-Fe-Fe	embedded single crystals
Pl20	1150	100	42100	2.7 ± 0.4	42500	<11	Ni-Fe-Fe	
Pl27	1150	200	77900	3.7 ± 0.9		<11	Ni-Fe-Fe	
Pl22	1150	300	37300	2.9 ± 0.6	28900	<11	Ni-Fe-Fe	
Pl29	1150	400	88100	4.1 ± 1.2		<11	Fe-Fe-Fe	

[a] T is temperature, P is pressure, C_{H2O} is water content, d is grain size.
[b] The sc denotes water content of single crystals.

Table 2. Creep Data of Wet Samples

P, MPa	T, °C	log (σ), MPa	log $\dot{\varepsilon}$, s^{-1}
		PL13	
100	1000	1.62	−6.25
100	1000	1.82	−5.91
100	1000	1.98	−5.61
100	1000	2.09	−5.38
100	1000	2.24	−5.08
100	1000	2.33	−4.88
100	1000	2.40	−4.75
100	1000	2.44	−4.64
100	1000	2.48	−4.50
		PL25	
300	1000	1.15	−5.32
300	1000	1.39	−5.09
300	1000	1.54	−4.94
300	1000	1.66	−4.82
300	1000	1.74	−4.72
300	1000	1.89	−4.59
300	1000	1.99	−4.48
300	1000	2.14	−4.31
300	1000	2.25	−4.16
300	1000	2.37	−3.93
300	1000	2.42	−3.79
300	1000	2.46	−3.66
		PL21	
400	1000	1.38	−4.73
400	1000	1.68	−4.42
400	1000	1.87	−4.23
400	1000	2.00	−4.13
400	1000	2.27	−3.79
400	1000	2.33	−3.66
400	1000	2.38	−3.57
400	1000	2.42	−3.46
400	1000	2.46	−3.31
		PL19	
100	1050	1.45	−5.38
100	1050	1.51	−5.31
100	1050	1.70	−4.99
100	1050	1.83	−4.77
		PL26	
300	1050	1.63	−5.06
300	1050	1.73	−4.90
300	1050	1.81	−4.79
300	1050	1.93	−4.60
300	1050	2.03	−4.49
300	1050	1.45	−5.29
300	1050	2.01	−4.50
300	1050	2.16	−4.30
300	1050	2.26	−4.11
300	1050	2.34	−3.95
300	1050	2.40	−3.79
300	1050	2.45	−3.65
		PL18	
400	1050	1.44	−4.61
400	1050	1.64	−4.35
400	1050	1.79	−4.19
400	1050	1.90	−4.10
400	1050	2.02	−3.97
400	1050	2.25	−3.65
400	1050	2.33	−3.51
400	1050	2.39	−3.36
400	1050	2.43	−3.23
400	1050	2.47	−3.06
		PL37	
150	1050	1.59	−3.74
150	1050	1.72	−3.65
150	1050	1.81	−3.55
150	1050	1.91	−3.40
300	1050	1.58	−3.64
300	1050	1.75	−3.52
300	1050	1.83	−3.44
300	1050	1.92	−3.33
450	1050	1.43	−3.55
450	1050	1.66	−3.34
450	1050	1.80	−3.18
450	1050	1.91	−3.07
		PL36	
150	1050	1.66	−3.71
150	1050	1.81	−3.60
150	1050	1.92	−3.47
300	1050	1.75	−3.67
300	1050	1.86	−3.61
300	1050	1.95	−3.51
300	1050	2.39	−2.55
300	1050	2.40	−2.50
450	1050	1.50	−3.68
450	1050	1.61	−3.58
450	1050	1.73	−3.49
450	1050	1.85	−3.37
450	1050	1.95	−3.31
		PL34	
150	1050	1.99	−4.30
150	1050	2.26	−4.01
150	1050	2.31	−3.96
150	1050	2.35	−3.85
150	1050	2.41	−3.69
300	1050	2.02	−4.30
300	1050	2.28	−3.98
300	1050	2.33	−3.91
300	1050	2.38	−3.83
300	1050	2.43	−3.72
450	1050	2.05	−4.37
450	1050	2.30	−3.99
450	1050	2.36	−3.92
450	1050	2.41	−3.89
450	1050	2.46	−3.73
		PL33	
150	1050	1.66	−4.90
150	1050	1.81	−4.80
150	1050	1.92	−4.71
150	1050	2.01	−4.60
300	1050	1.68	−4.92
300	1050	1.83	−4.76
300	1050	1.94	−4.65
300	1050	2.02	−4.56
450	1050	1.68	−4.96
450	1050	1.82	−4.77
450	1050	1.93	−4.64
450	1050	2.03	−4.50
		PL35	
300	1050	1.73	−5.22
300	1050	1.85	−5.13
300	1050	1.96	−4.94
300	1050	2.04	−4.85
450	1050	1.71	−5.21
450	1050	1.85	−5.10
450	1050	1.95	−4.94
450	1050	2.05	−4.80
		PL32	
300	1050	1.96	−4.00
300	1050	2.39	−3.22
300	1050	2.44	−3.10
300	1050	2.46	−3.01
450	1050	2.01	−4.34
450	1050	2.46	−3.51
450	1050	2.51	−3.33

Table 2. (continued)

P, MPa	*T*, °C	log (σ), MPa	log $\dot{\varepsilon}$, s^{-1}
450	1050	2.54	−3.16
		PL17	
100	1100	1.74	−4.88
100	1100	1.87	−4.72
100	1100	1.97	−4.60
100	1100	2.09	−4.45
100	1100	2.25	−4.19
100	1100	2.34	−4.00
100	1100	2.41	−3.79
100	1100	2.46	−3.60
100	1100	2.53	−3.24
		PL14	
200	1100	1.72	−4.50
200	1100	1.77	−4.44
200	1100	1.84	−4.35
200	1100	1.95	−4.24
200	1100	2.07	−4.10
200	1100	2.29	−3.74
200	1100	2.36	−3.57
200	1100	2.42	−3.38
200	1100	2.47	−3.21
200	1100	2.51	−3.00
		PL15	
300	1100	1.70	−4.47
300	1100	1.83	−4.30
300	1100	1.93	−4.21
300	1100	2.05	−4.07
300	1100	2.26	−3.72
300	1100	2.34	−3.55
300	1100	2.40	−3.38
300	1100	2.44	−3.24
300	1100	2.50	−3.05
		PL16	
400	1100	1.70	−4.66
400	1100	1.83	−4.49
400	1100	1.94	−4.40
400	1100	2.06	−4.27
400	1100	2.28	−3.97
400	1100	2.35	−3.83
400	1100	2.42	−3.69
400	1100	2.46	−3.58
400	1100	2.51	−3.45
		PL20	
100	1150	1.58	−4.01
100	1150	1.74	−3.82
100	1150	1.87	−3.67
100	1150	1.96	−3.54
100	1150	2.19	−2.98
100	1150	2.25	−2.69
		PL27	
200	1150	0.92	−5.05
200	1150	1.13	−4.84
200	1150	1.27	−4.69
200	1150	1.39	−4.58
200	1150	1.47	−4.49
200	1150	1.54	−4.41
200	1150	1.60	−4.34
200	1150	1.70	−4.22
200	1150	1.78	−4.12
200	1150	1.90	−3.94
200	1150	2.04	−3.73
200	1150	2.14	−3.54
200	1150	2.24	−3.29
200	1150	2.32	−3.05
200	1150	2.38	−2.81

Table 2. (continued)

P, MPa	*T*, °C	log (σ), MPa	log $\dot{\varepsilon}$, s^{-1}
		PL22	
300	1150	1.48	−4.20
300	1150	1.59	−4.07
300	1150	1.75	−3.87
300	1150	1.87	−3.70
300	1150	1.96	−3.60
300	1150	2.21	−3.25
300	1150	2.33	−2.98
300	1150	2.35	−2.89
300	1150	2.40	−2.73
		PL29	
400	1150	0.89	−5.01
400	1150	1.25	−4.62
400	1150	1.46	−4.39
400	1150	1.08	−4.79
400	1150	1.35	−4.52
400	1150	1.43	−4.43
400	1150	1.50	−4.35
400	1150	1.56	−4.29
400	1150	1.66	−4.19
400	1150	1.74	−4.09
400	1150	1.87	−3.94
400	1150	1.97	−3.81
400	1150	2.12	−3.60
400	1150	2.23	−3.40
400	1150	2.31	−3.21
400	1150	2.43	−2.84

domains. Hydrous samples contain more residual glass and Si-enriched melt located in triple junctions. Wetting of grain boundaries was not observed. Intracrystalline fluid inclusions are frequently surrounded by glass. The total melt content is estimated to be $\lesssim$1 vol %. Interestingly, intracrystalline fluid inclusions are also frequently found in dry samples. This suggests that solubility of water-related point defects in the synthetic anorthite may be lower than that of embedded single crystals at experimental conditions. Similarly, *Dresen et al.* [1996] found that anorthite crystallized from a glass containing about 200 ppm H/Si displayed numerous fluid inclusions. The authors suggested that fluid inclusions containing H_2O likely exsolved during crystallization at 0.1 MPa pressure and >1000°C.

2.4. Experimental Deformation and Data Analysis

[12] We performed deformation experiments in a Paterson-type gas deformation apparatus on both dry and wet feldspar specimens to investigate the effect of activation volume and water fugacity on sample strength. Dry samples were jacketed using a ∼0.35 mm thick iron sleeve and deformed in a standard gas deformation apparatus assembly [*Paterson*, 1990]. For deformation tests at hydrous conditions the standard sample assembly inside the iron sleeve consisted of a thin nickel foil wrapped around the sample, surrounded by a 0.85 mm thick pyrophyllite sleeve, and enclosed in a sealed steel capsule [*Mei and Kohlstedt*, 2000a], referred to in the following as NFF assembly (abbreviation for Ni foil–Fe capsule–Fe jacket). Gas-tight sealing of the capsule was ensured by careful laser welding. Pyrophyllite dehydrates above a temperature of about 400 °C at 300 MPa pressure, releasing ∼5 wt % H_2O. If the anorthite aggregates would incorporate the released water completely they would contain about 2.9 wt %. The

Table 3. Creep Data of Dry Samples

P, MPa	T, °C	log (σ), MPa	log $\dot{\varepsilon}$, s^{-1}
		PL23	
100	1125	1.57	−5.99
100	1125	1.69	−5.90
100	1125	2.00	−5.63
100	1125	2.09	−5.57
100	1125	2.20	−5.44
100	1125	2.34	−5.24
100	1125	2.48	−5.09
100	1125	2.51	−5.04
200	1125	1.58	−6.06
200	1125	1.78	−5.89
200	1125	1.88	−5.82
200	1125	1.98	−5.74
200	1125	2.17	−5.56
200	1125	2.46	−5.28
200	1125	2.48	−5.27
200	1125	2.51	−5.25
300	1125	1.87	−5.89
300	1125	2.01	−5.80
300	1125	2.09	−5.76
300	1125	2.22	−5.67
300	1125	2.35	−5.52
300	1125	2.45	−5.41
300	1125	2.48	−5.39
300	1125	2.51	−5.36
300	1125	2.54	−5.31
300	1125	2.56	−5.27
400	1125	1.70	−6.13
400	1125	1.79	−6.09
400	1125	1.92	−5.98
400	1125	2.06	−5.80
400	1125	2.19	−5.63
400	1125	2.39	−5.38
400	1125	2.45	−5.31
400	1125	2.50	−5.21
400	1125	2.55	−5.12
400	1125	2.59	−5.07
		PL30	
100	1140	1.56	−5.29
100	1140	1.78	−5.13
100	1140	1.92	−5.03
100	1140	2.03	−4.96
100	1140	2.15	−4.89
100	1140	2.24	−4.82
100	1140	2.32	−4.74
100	1140	2.38	−4.61
100	1140	2.43	−4.47
200	1140	1.55	−5.35
200	1140	1.77	−5.19
200	1140	1.92	−5.10
200	1140	2.02	−5.03
200	1140	2.14	−4.93
200	1140	2.24	−4.86
200	1140	2.31	−4.80
200	1140	2.38	−4.73
200	1140	2.43	−4.68
300	1140	1.56	−5.27
300	1140	1.77	−5.18
300	1140	2.02	−5.04
300	1140	2.14	−4.97
300	1140	2.23	−4.91
300	1140	2.35	−4.80
300	1140	2.43	−4.72
300	1140	2.47	−4.65
400	1140	1.78	−5.41
400	1140	1.93	−5.32
400	1140	2.03	−5.25
400	1140	2.15	−5.13
400	1140	2.25	−5.05
400	1140	2.37	−4.90
400	1140	2.44	−4.79
400	1140	2.49	−4.71

Table 3. (continued)

P, MPa	T, °C	log (σ), MPa	log $\dot{\varepsilon}$, s^{-1}
400	1140	2.53	−4.64
		PL07	
100	1150	1.90	−4.69
100	1150	2.00	−4.63
200	1150	1.93	−4.76
200	1150	2.11	−4.66
200	1150	2.25	−4.53
200	1150	2.47	−3.77
200	1150	2.50	−3.75
200	1150	2.52	−3.70
300	1150	1.93	−4.80
300	1150	2.10	−4.69
300	1150	2.24	−4.56
300	1150	2.49	−3.87
300	1150	2.52	−3.85
300	1150	2.55	−3.80
400	1150	1.94	−4.78
400	1150	2.11	−4.64
400	1150	2.25	−4.49
400	1150	2.46	−4.23
400	1150	2.49	−4.19
400	1150	2.52	−4.10
400	1150	2.56	−4.01
Pl24			
100	1160	1.90	−4.77
100	1160	2.04	−4.66
100	1160	2.15	−4.55
100	1160	2.26	−4.40
100	1160	2.42	−3.93
100	1160	2.45	−3.74
100	1160	2.48	−3.56
100	1160	2.50	−3.35
200	1160	1.90	−4.79
200	1160	2.04	−4.70
200	1160	2.15	−4.62
200	1160	2.26	−4.50
200	1160	2.42	−4.26
200	1160	2.45	−4.22
200	1160	2.48	−4.18
200	1160	2.51	−4.12
200	1160	2.53	−4.09
300	1160	2.03	−4.77
300	1160	2.13	−4.69
300	1160	2.24	−4.59
300	1160	2.40	−4.40
300	1160	2.43	−4.37
300	1160	2.46	−4.33
300	1160	2.49	−4.29
300	1160	2.51	−4.25
400	1160	1.92	−5.16
400	1160	2.01	−5.04
400	1160	2.12	−4.92
400	1160	2.21	−4.83
400	1160	2.31	−4.72
400	1160	2.45	−4.51
400	1160	2.50	−4.43
400	1160	2.54	−4.35
400	1160	2.57	−4.26
400	1160	2.60	−4.18
		PL06_1	
200	1175	1.84	−4.42
200	1175	1.95	−4.36
200	1175	2.08	−4.26
200	1175	2.30	−4.02
200	1175	2.44	−3.80
200	1175	2.50	−3.64
200	1175	2.52	−3.55
200	1175	2.54	−3.46
300	1175	1.95	−4.44
300	1175	2.08	−4.36

Table 3. (continued)

P, MPa	T, °C	log (σ), MPa	log $\dot{\varepsilon}$, s^{-1}
300	1175	2.30	−4.12
300	1175	2.44	−3.88
300	1175	2.50	−3.71
300	1175	2.52	−3.61
300	1175	2.54	−3.51
		PL06_2	
400	1175	1.82	−4.56
400	1175	1.93	−4.48
400	1175	2.06	−4.37
400	1175	2.28	−4.12
400	1175	2.42	−3.88
400	1175	2.47	−3.72
400	1175	2.51	−3.58
400	1175	2.54	−3.45
		PL31	
200	1185	1.53	−4.93
200	1185	1.66	−4.88
200	1185	1.75	−4.83
200	1185	1.90	−4.71
200	1185	2.00	−4.64
200	1185	2.13	−4.49
200	1185	2.22	−4.36
200	1185	2.30	−4.25
200	1185	2.36	−4.14
300	1185	1.55	−5.07
300	1185	1.76	−4.92
300	1185	1.91	−4.83
300	1185	2.01	−4.77
300	1185	2.13	−4.67
300	1185	2.23	−4.59
300	1185	2.30	−4.51
300	1185	2.37	−4.40
300	1185	2.42	−4.32
400	1185	1.63	−5.36
400	1185	1.78	−5.26
400	1185	1.92	−5.16
400	1185	2.03	−5.09
400	1185	2.15	−4.97
400	1185	2.24	−4.87
400	1185	2.32	−4.77
400	1185	2.38	−4.68
400	1185	2.47	−4.53
400	1185	2.51	−4.44
400	1185	2.55	−4.35
		PL08	
200	1200	1.87	−4.35
200	1200	2.01	−4.27
200	1200	2.11	−4.20
200	1200	2.22	−4.08
200	1200	2.36	−3.50
200	1200	2.41	−3.45
200	1200	2.45	−3.39
200	1200	2.49	−3.30
300	1200	1.87	−4.35
300	1200	2.01	−4.27
300	1200	2.12	−4.18
300	1200	2.35	−3.49
300	1200	2.39	−3.45
300	1200	2.44	−3.39
300	1200	2.47	−3.30
400	1200	1.88	−4.40
400	1200	2.02	−4.27
400	1200	2.15	−4.14
400	1200	2.36	−3.80
400	1200	2.41	−3.73
400	1200	2.45	−3.63
400	1200	2.49	−3.53

jacketing materials served as solid buffers setting oxygen fugacity during deformation of wet (Ni-NiO) and dry (Fe-FeO) samples [*Mei and Kohlstedt*, 2000a]. A few samples were buffered using metal sleeves prepared entirely from nickel, iron or copper, respectively (Table 1).

[13] To correct load for the strength of metal and pyrophyllite sleeves, we ran calibration experiments on dummy samples from similar material or used published flow laws [*Frost and Ashby*, 1982]. The deformation apparatus is equipped with an internal furnace, load cell, and LVDT. Temperature uncertainty is less than 0.5%. Stress was calculated assuming constant volume deformation. We give true (natural) strain determined from the measurement of axial displacement and corrected for system compliance. Sensor-related accuracy of axial stress is 0.6% and of strain rate 0.3%. During the course of an experiment uncertainty of calculated stress increases by 0.6% due to uncertainty of applied jacket correction, 0.8% due to the pressure sensitivity of the load cell for small confining pressure fluctuations, and ∼2% due to sample bulging. Precision of measured initial sample diameter yields another 1% uncertainty. In total, accuracy of stress is 3% and in few cases 5%.

[14] Specimens were usually annealed for 17 h at test conditions before starting deformation runs to allow for equilibration with thermodynamic conditions and chemical environment. All samples were deformed at constant load with a stepwise increase of the axial load for a single sample at constant temperature (creep testing). Strain per step was between 1.3 and 2.1% and secondary creep at constant rate was usually achieved after straining for about 0.5%. Increase of sample diameter during axial shortening results in about 2% uncertainty of reported "constant" stress values and "steady state" creep rates. No correction for grain growth was required as grain size of deformed samples is comparable to undeformed specimens.

[15] A total of 20 hydrous samples were deformed at $T = 1000–1150°C$, pressures between 100 and 450 MPa, and stresses of ∼10–340 MPa, yielding steady state strain rates of $\sim 6 \times 10^{-7}$ to 3×10^{-3} s^{-1} (Table 2). For 14 samples, confining pressure was maintained constant and 6 samples were deformed at a stepwise reduced pressure.

[16] Eight dry samples were coaxially deformed at temperatures of 1125°–1200°C, confining pressures stepwise reduced from 400 to 100 MPa, and axial stresses between ∼30 and 400 MPa, resulting in axial strain rates of about 7×10^{-7} to 5×10^{-4} s^{-1} (Table 3). Two dry specimens (Pl07 and Pl08) were first deformed at low stresses (200 MPa) and stepwise reduced confining pressure. Samples were then loaded to higher stresses and deformed with similar pressure steps. After deformation at each pressure step the remaining dry samples were elongated to the original length over night by low stress extension. This procedure allowed performing several tests at different conditions on a single specimen. Sample Pl06 was cut in two parts that were tested at different pressures. For all samples, annealing time after pressure stepping was at least 2 hours to allow for reequilibration.

3. Results

3.1. Mechanical Data

[17] Specimens deformed at hydrous conditions are weaker than dry samples. Stress-strain rate data of the

deformed wet and dry rock samples reveal lower viscosities with increasing temperature (Tables 2 and 3). However, small variations in microstructure, grain size and water content significantly affect the deformation behavior. The experimental data are fit to a power law of the form

$$\dot{\varepsilon} = A\sigma^n \exp\left[-\frac{Q+pV}{RT}\right] d^{-m} f_{H_2O}^r f_{H/O_2}^w \quad (1)$$

where $\dot{\varepsilon}$ is strain rate, A is a material constant, σ is stress, n is stress exponent, Q is activation energy, p is pressure, V is activation volume, T is absolute temperature, R is the molar gas constant, d is grain size, m is grain size exponent, f_{H_2O} is water fugacity, f_{H/O_2} is fugacity of hydrogen/oxygen, and r, w are fugacity exponents [*Evans and Kohlstedt*, 1995; *Mei and Kohlstedt*, 2000a; *Paterson*, 1989]. Theoretical models of grain boundary and lattice diffusion - controlled creep predict $m = 3$ and $m = 2$, respectively with a stress exponent of $n = 1$. For climb-controlled dislocation creep, deformation is commonly assumed to be grain size insensitive ($m = 0$) with a stress exponent of $n = 3–5$ [*Chokshi and Langdon*, 1991]. If individual deformation mechanisms operate independently and in parallel, strain rates add at given stress and the fastest mechanism is expected to dominate the bulk creep behavior.

[18] At stresses $\lesssim$200 MPa for anhydrous samples and stresses $\lesssim$100 MPa for wet specimens, deformation was linear viscous with $n \approx 1$ suggesting diffusion-controlled creep. At higher stresses we observed a gradual transition to dislocation creep with $n > 2$ (Figure 1). When stresses are significantly higher than the confining pressure, creep rates accelerated due to microfracturing of the samples. In this paper we only discuss mechanical data obtained in the low stress region.

[19] At anhydrous conditions the viscosity of anorthite aggregates increases with increasing confining pressure although the data shows some scatter (Figure 1a and Table 3). To estimate flow law parameters, we assumed $n = 1$ and $m = 3$ as suggested by previous studies on grain boundary diffusion-controlled creep of fine-grained feldspar aggregates [see *Rybacki and Dresen*, 2000, and references therein]. At dry

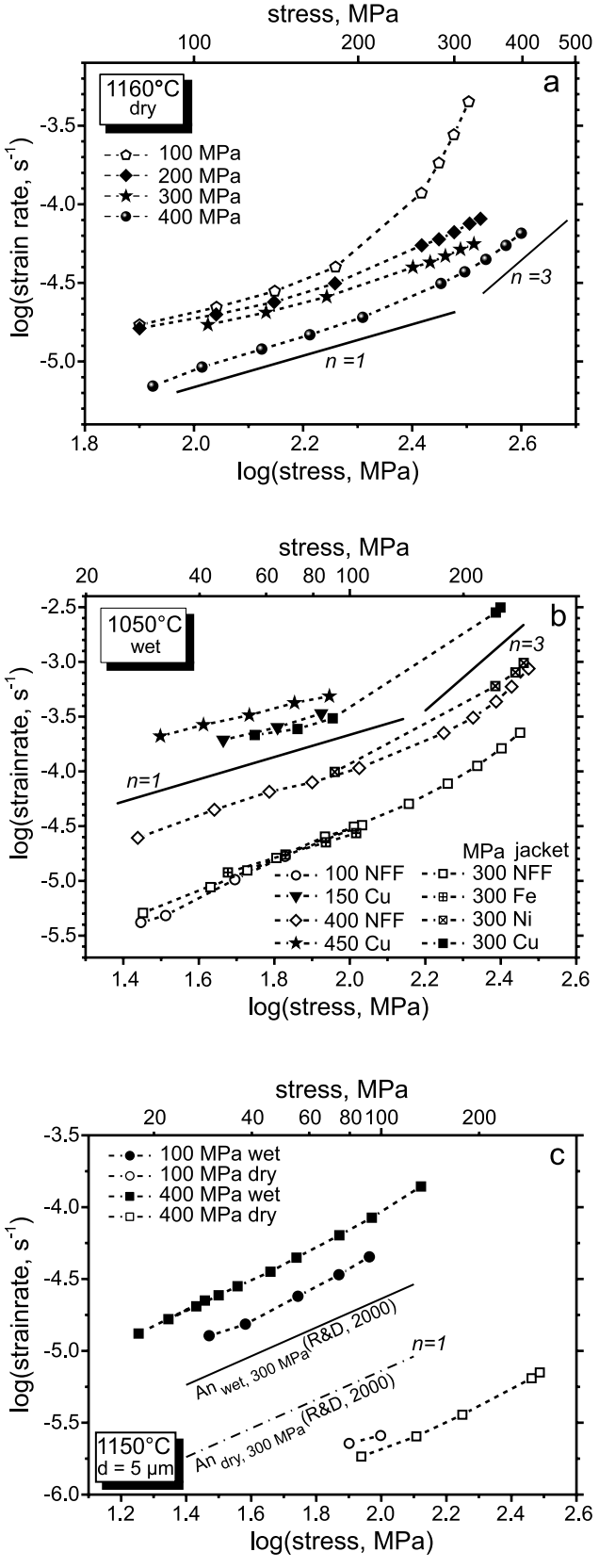

Figure 1. Representative stress-strain curves for high-temperature creep of fine-grained anorthite aggregates. In log-log scale the curves reveal a gradual transition from Newtonian flow (stress exponent $n = 1$) at low stresses to power law creep ($n \approx 3$) at high stresses, indicating a transition from diffusion-accommodated creep to dislocation creep. (a) Dry samples are stronger with increasing pressure. Note the accelerated creep at high stress and 100 MPa confining pressure, indicating the onset of tertiary creep (sample Pl24, T = 1160°C). (b) Wet samples usually show enhanced creep rate with increasing pressure. At given pressure and temperature (e.g., 300 MPa, 1050°C), samples buffered by Cu-CuO (solid symbols, sample Pl36)) are considerably weaker than those buffered by Ni-NiO and Fe-FeO (crossed squares, samples Pl32 and Pl33, respectively) and specimens buffered by Ni-Fe-Fe (NFF, open symbols, samples Pl19, Pl26, and Pl18). (c) At 1150°C, dry samples (Pl07) are about 1.5 orders of magnitude stronger than wet samples (Pl20, Pl29). For comparison, the creep curves for grain boundary diffusion of synthetic anorthite obtained at 300 MPa pressure [*Rybacki and Dresen*, 2000] are shown. Data are normalized to 5 μm grain size.

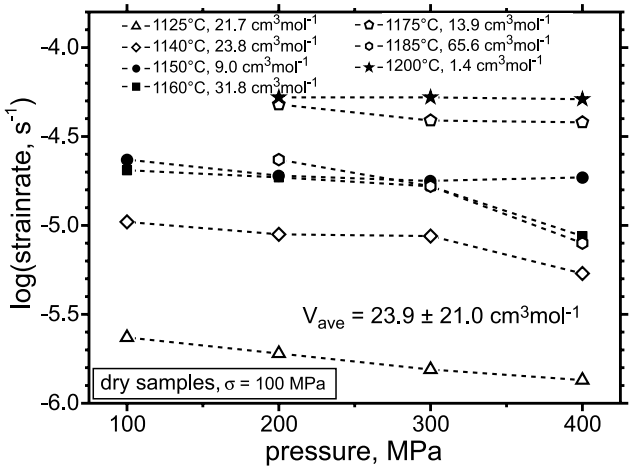

Figure 2. The log (strain rate) versus confining pressure for dry samples at 100 MPa axial stress (diffusion creep regime). For each temperature the slope of curve determines the activation volume V under dry conditions. Solid symbols denote samples with about 10 times higher bulk water content than those indicated by open symbols (compare Table 1). The average activation volume is 24 ± 21 cm^3 mol^{-1}.

conditions fugacity exponents are assumed r, w = 0. A multilinear regression fit to the data at stresses <210 MPa yields an activation energy of Q = 482 ± 41 kJ mol^{-1} and a preexponential factor of log(A) = 12.4 ± 1.5 MPa^{-1} μm^3 s^{-1}. This is in good agreement with results of *Rybacki and Dresen* [2000] for dry synthetic anorthite aggregates (Q = 467 ± 16 kJ mol^{-1} and log(A) = 12.1 ± 0.6 MPa^{-1}μm^3 s^{-1}).

[20] At hydrous conditions strain rates generally increase with increasing confining pressure (Figure 1b and Table 2). Interestingly, samples buffered by Cu-CuO are about 1 order of magnitude weaker than specimens buffered by Ni-NiO or Fe-FeO at a pressure of 300 MPa and 1050°C. The creep strength of samples buffered in the NFF assembly is very similar to that of Fe-buffered samples. Two samples were buffered by Ni-NiO. Their data show a large scatter and samples failed at low confining pressure (150 MPa, Table 2). At 1150°C temperature dry samples are more than 1 order of magnitude stronger than wet specimens (Figure 1c).

3.2. Activation Volume of Anhydrous Samples

[21] Determination of the activation volume V from diffusion creep data of individual specimens for a single temperature shows considerable scatter of V between 1.4 cm^3 mol^{-1} and 65.6 cm^3 mol^{-1} (Figure 2). Averaging over the entire data set yields V = 23.9 ± 21.0 cm^3 mol^{-1}, corresponding to a pressure-dependent change of the apparent activation energy $Q_{app} = Q + pV$ of 2.4 kJ mol^{-1} per 100 MPa. In comparison, using a multilinear regression fit to the data yields an activation volume V of 32.4 ± 6.6 cm^3 mol^{-1}. However, we believe that the averaging approach better reflects the large uncertainty involved in our estimates of the activation volume due to the relatively small pressure range accessible in the gas apparatus. For example, uncertainty in grain size of about 10% results in an uncertainty of 10 cm^3 mol^{-1} for the activation volume at the experimental conditions commonly used in the gas apparatus.

[22] No significant difference in activation volume is found for samples fabricated from coarse-grained starting powders (solid symbols in Figure 2) and specimens produced from fine-grained powder containing about 10 times less water.

3.3. Activation Volume and Water Fugacity Exponent of Hydrous Samples

[23] Water fugacity values were calculated following *Churakow and Gottschalk* [2003a, 2003b] and *Gottschalk* [1997]. For the standard NFF assembly we expect that the fugacity is buffered near Fe-FeO. *Mei and Kohlstedt* [2000a] used a similar assembly to buffer deformation experiments on olivine at Ni-NiO. However, using X-ray diffraction analysis and optical inspection we never found clear evidence for the formation of NiO after deformation.

[24] We used two different approaches to obtain the water fugacity exponent for creep of hydrous feldspar aggregates. On the basis of the results of *Rybacki and Dresen* [2000] for diffusion creep of similar wet anorthite aggregates we set the stress exponent to n = 1, the grain size exponent to m = 3, and the activation energy to Q = 170 kJ mol^{-1}. Using a three-dimensional (3-D) fit program (Table Curve 3D, SPSS Inc.) allows determining water fugacity exponent and activation energy simultaneously. We ignored 4 data points from a failed run of sample PL13. A fit of 101 data yields a water fugacity exponent of r = 0.98 and an activation volume of V = 36.4 cm^3 mol^{-1}. However, the fit also depends on the preexponential constant A and shows several local minima of the residuals.

[25] In an additional approach to constrain the water fugacity exponent we assume that the activation volume determined for dry rocks provides a lower bound for the activation volume of diffusion creep at hydrous conditions. Taking V = 24 cm^3 mol^{-1}, the water fugacity exponent

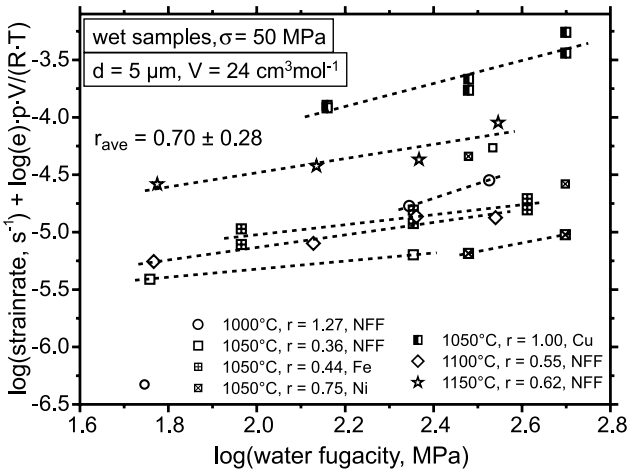

Figure 3. The log (strain rate) plotted versus log (water fugacity) for wet samples at 50 MPa axial stress (diffusion creep regime) for an assumed activation volume of 24 cm^3 mol^{-1}. The average water fugacity exponent r is 0.70 ± 0.28. Small symbols were not considered for fitting. Abbreviations denote jacketing materials (NFF = Ni-Fe-Fe). Data are corrected for 5 μm grain size.

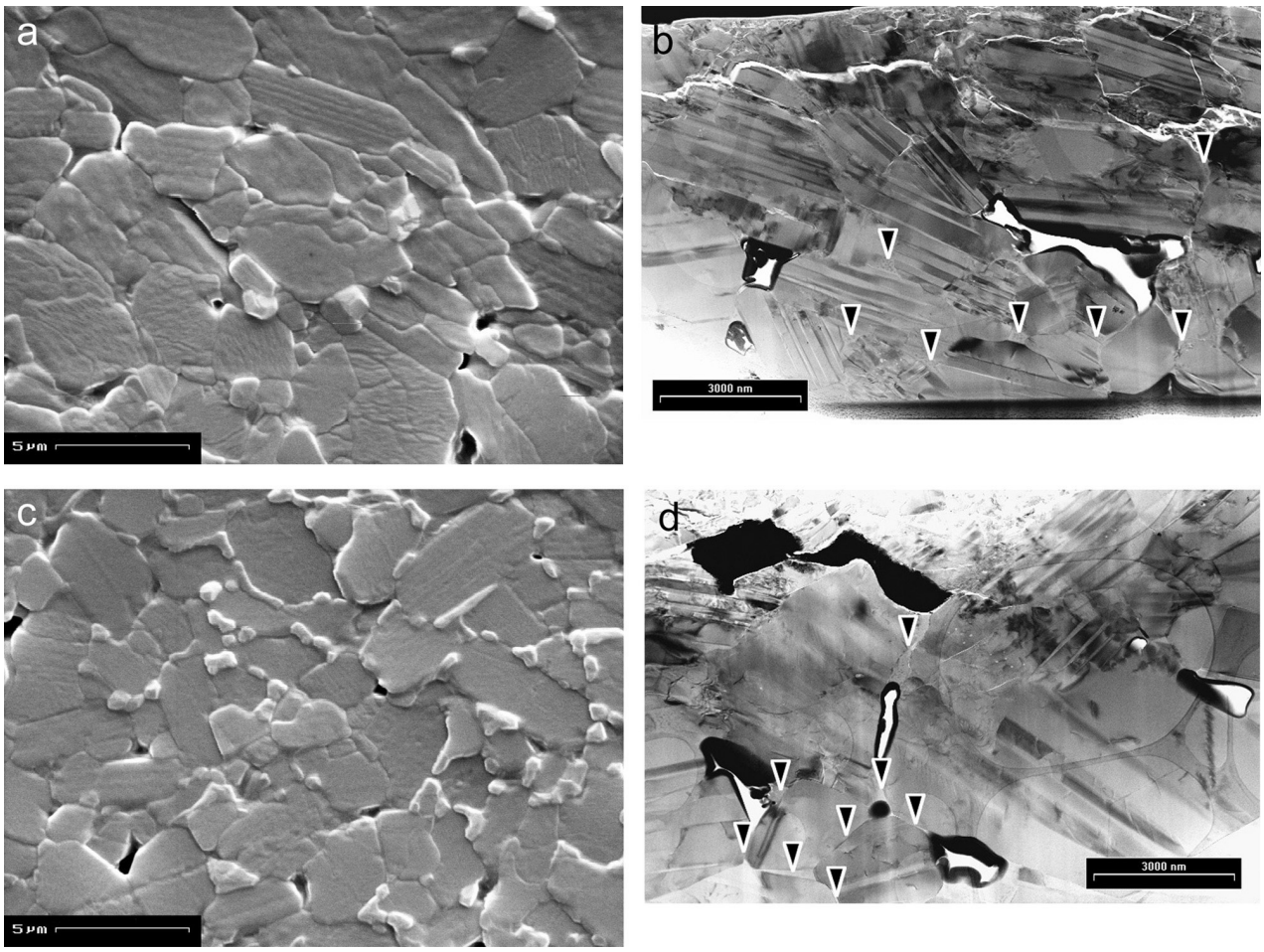

Figure 4. Micrographs of deformed samples. (a) and (b) SEM and (FIB-)TEM sections of Fe-jacketed sample Pl34 are shown, and (c) and (d) SEM and (FIB-)TEM sections of Cu-jacketed sample Pl36 are shown, both deformed at 1050°C. Pores appear as black holes in SEM and white areas, surrounded by Ga deposits from ion beaming, in TEM, respectively. The small fractures visible at the top of TEM micrographs result from saw cutting. SEM sections were thermally etched to separate grain boundaries. The two large black areas in the upper left quarter of Figure 4d are Cu deposits. Note grain boundaries and triple junctions containing glass in Cu-jacketed sample.

estimated for the low-stress diffusion creep regime is $r = 0.7 \pm 0.3$ (Figure 3). Assuming the NNF assemblies were buffered by Ni-NiO instead of Fe-FeO changes the average water fugacity exponent by $<\pm 0.1$.

[26] The calculated water fugacities may have been affected by the presence of dissolved carbon from the steel jackets, decreasing the reported values by ~40–60% in the investigated P-T range [*Connolly and Cesare*, 1993]. However, the grayish coloration of sample rims and X-ray analysis of the samples using Rietveld refinement show that only the outermost rims are contaminated.

3.4. Water Content

[27] After deformation the hydroxyl content of samples deformed at hydrous conditions remained similar to the starting material or increased only slightly. The average water content was 0.33 ± 0.14 wt % H_2O, or 51000 ± 21000 ppm H/Si (Table 1). For one sample a water content of ~0.3 wt % was also estimated by Raman spectroscopy in the wave number range of 3100–3750 cm^{-1}. FTIR spot measurements along profiles with 20 µm spacing show a sixfold increase in water content from embedded anorthite single crystals toward the fine-grained matrix. This indicates that a significant amount of hydroxyl is stored in grain boundaries. A similar finding was reported by *Mei and Kohlstedt* [2000a] in a study on olivine, where these authors found a 15–20 times higher bulk water concentration than in olivine single crystals. Notably, *Mei and Kohlstedt* [2000a] also reported an increase of bulk water content with increasing confining pressure, which we did not observe in our samples. This observation and the abundance of fluid inclusions in the anorthite matrix suggest that samples were possibly oversaturated even in the absence of pyrophyllite. The anorthite single crystals did not incorporate significantly higher hydroxyl content with increasing pressure. However, diffusion kinetics of water related species in anorthite are not well known. As a first estimate, *Dimanov et al.* [1999] report a diffusion coefficient D of about 10^{-15} m^2 s^{-1} for volume diffusion of water in anorthite at $T = 1150$°C, the highest temper-

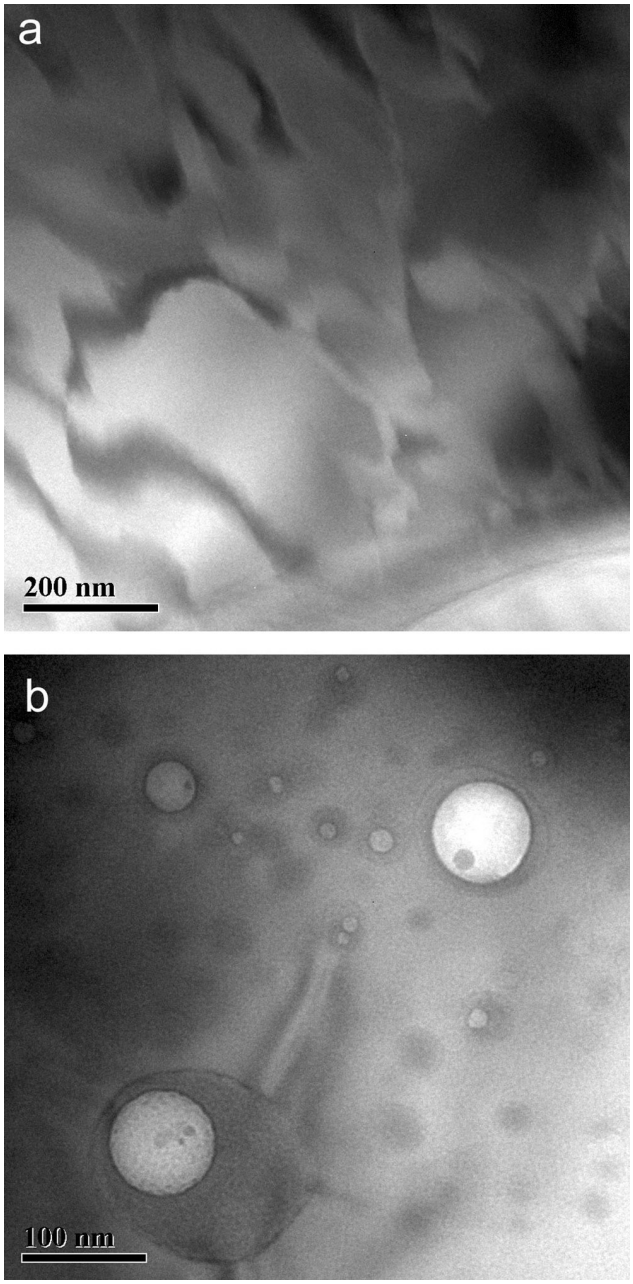

Figure 5. TEM micrographs showing (a) antiphase domains and (b) fluid inclusions surrounded by melt rims (sample Pl36).

ature attained in our experiments. With the relation $d = \sqrt{2Dt}$ the equilibrium distance **d** is about 12 μm for a typical experiment of t = 20 hour duration including annealing time prior to testing. For comparison, *Paterson and Luan* [1990] estimated $d \approx 7$ μm for volume diffusion of water in quartz at similar conditions. This short distance suggests that the duration of experiments was too short for the water content of the embedded large single crystals to fully equilibrate with pressure.

3.5. Microstructures

[28] The grain size of deformed samples did not change significantly compared to the starting material. Grains are often prismatic with relatively straight boundaries forming 120° triple junctions. Frequently grains are twinned but show few dislocations (Figure 4). Wet samples locally show antiphase domains, shells of amorphous material surrounding fluid inclusions, and Si-enriched glass in triple junctions (Figures 5 and 6). The glass present in triple junctions is commonly depleted in Ca and Al and is not found along grain boundaries. Si enrichment may result from local nonstoichiometry of the starting glass but is more likely due to partial melting at high water fugacity. The total amount of glass estimated from large, FIB-prepared TEM foils is about 1–2 vol %. Samples that were significantly weaker like the specimens deformed in copper jackets showed glass films contained in grain boundaries interconnecting separate larger glass pockets in triple junctions. The glass is enriched in Si. Interestingly, interfacial angles estimated at grain triple junctions are about 40° ± 10° irrespective of the wetting behavior of the glass (Figures 6 and 7).

4. Discussion

4.1. Activation Volume

[29] At anhydrous conditions we estimate an activation volume V for diffusion-controlled creep of anorthite aggregates of 24 ± 21 cm^3 mol^{-1}. To our knowledge, no other measurements of V for grain boundary or volume diffusion in plagioclase are available to date [e.g., *Bejina et al.*, 2003]. However, the activation volume can be estimated roughly relating V to the pressure dependence of the melting temperature T_m:

$$V = \frac{Q}{T_m}\frac{dT_m}{dP}. \tag{2}$$

Using the pressure sensitivity of T_m for anhydrous anorthite given by *Holland and Powell* [2001] and the activation energy for diffusion creep of dry anorthite samples by *Rybacki and Dresen* [2000] results in an activation volume of $V \approx 6$ cm^3 mol^{-1}.

[30] Local elastic shear and volume distortions surrounding point defects result in pressure sensitivity of the shear modulus G and bulk modulus K, respectively. This allows estimating the activation volume for diffusion:

$$V = E\left(\frac{1}{G}\frac{dG}{dP} - \frac{1}{K}\right) \quad V = E\left(\frac{1}{K}\frac{dK}{dP} - \frac{1}{K}\right) \tag{3}$$

Using the elastic constants of anorthite and their pressure derivatives [*Sobolev and Babeyko*, 1994], we have $V \approx 24$–29 cm^3 mol^{-1} for dry aggregates in good agreement with our measured value of 24 cm^3 mol^{-1}.

[31] In the intrinsic diffusion regime the activation volume is the sum of point defect formation and migration, where the first term can be approximated by equation (2) and the second by equation (3) [*Bejina et al.*, 2003; *Karato*, 1981]. Although these are only rough estimates the resulting values suggest that the migration-related term dominates. The activation volume for diffusion creep of dry feldspar is close to estimates for high-temperature creep of other silicates. For dry dunite, *Kohlstedt and Wang* [2001] obtained $V \approx 20$ cm^3 mol^{-1} and for dry olivine aggregates

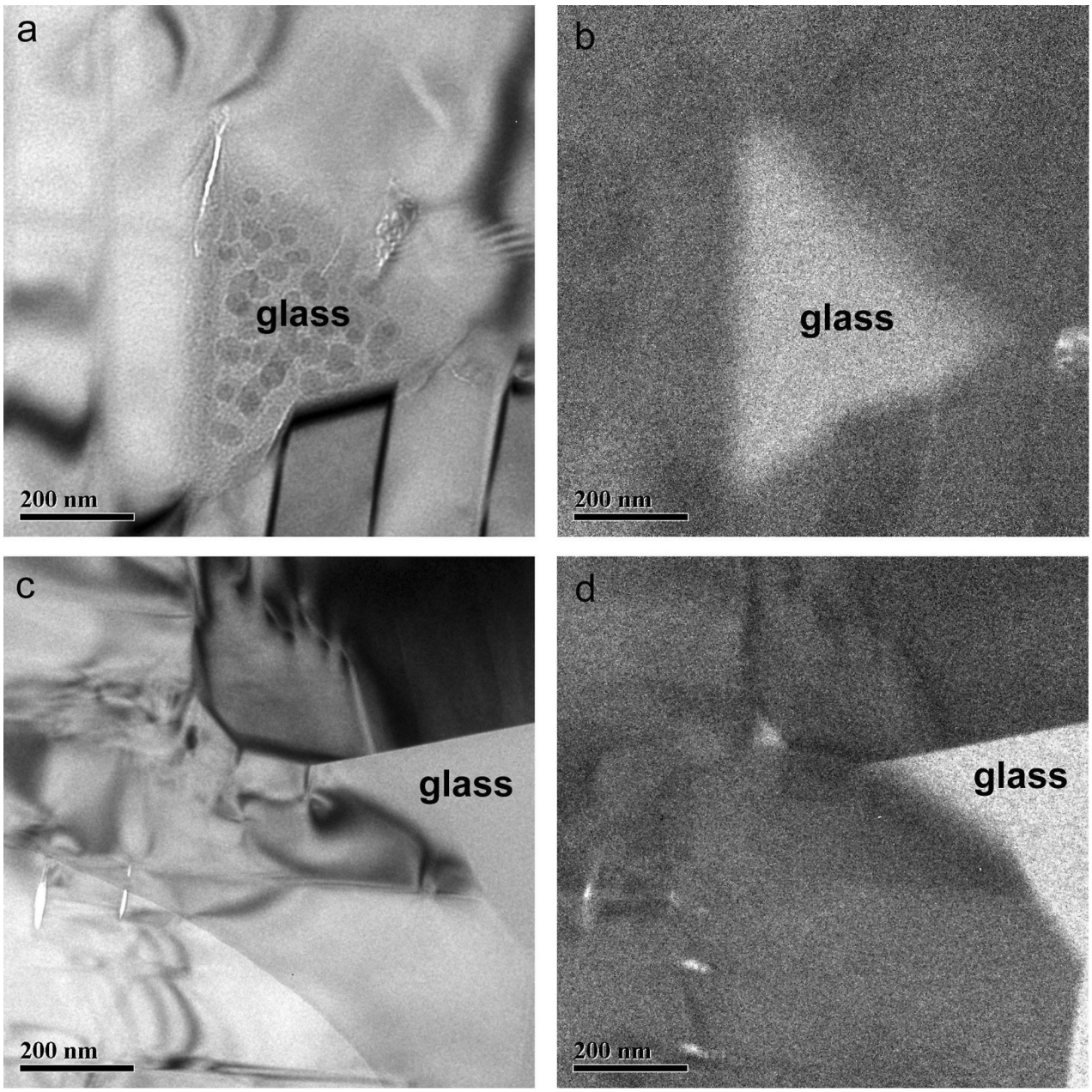

Figure 6. TEM micrographs of deformed samples Pl34 (Figures 6a and 6b) and Pl26 (Figures 6c and 6d), showing the topology of melt pockets. Pl34 was Fe-jacketed and Pl26 was NFF-jacketed. (a) and (c) Bright field are shown, and (b) and (d) dark field images are shown. Note the high apparent "wetting angle" of the amorphous phase. Both samples were deformed at 1050°C.

the creep activation volume is $V = 15 \pm 5$ cm^3 mol^{-1} [*Karato and Rubie*, 1997].

[32] Under wet conditions we obtained an activation volume of about 36 cm^3 mol^{-1} and $r = 0.98$ from a multiparameter fit to the data. Assuming that V estimated for dry samples forms a lower bound to V for wet feldspar this yielded a fugacity exponent of $r = 0.7$. We further assume that under wet conditions the relatively small ionic radius of protons incorporated in the crystal lattice and grain boundaries do not significantly affect the formation and migration volume of larger, potentially rate-controlling defects, like Si. The reaction of dry to water-bearing anorthite requires a volume change due to incorporation of protons. This allows estimating the activation volume for (proton-related) defect formation V_f. We estimate V_f for the following four defect mechanisms that may conceivably occur in a hydrous environment:

$$1\,Si^{4+} \rightleftharpoons 4\,H^{+},\ \text{formed by the reaction}\ 1\,CaAl_2Si_2O_8 + 4\,H_2O \rightleftharpoons 1\,CaAl_2H_8O_8 + 2\,SiO_2, \quad (4)$$

$$1\,Al^{3+} \rightleftharpoons 3\,H^{+},\ \text{from}\ 1\,CaAl_2Si_2O_8 + 3\,H_2O \rightleftharpoons 1\,CaH_6Si_2O_8 + 1\,Al_2O_3, \quad (5)$$

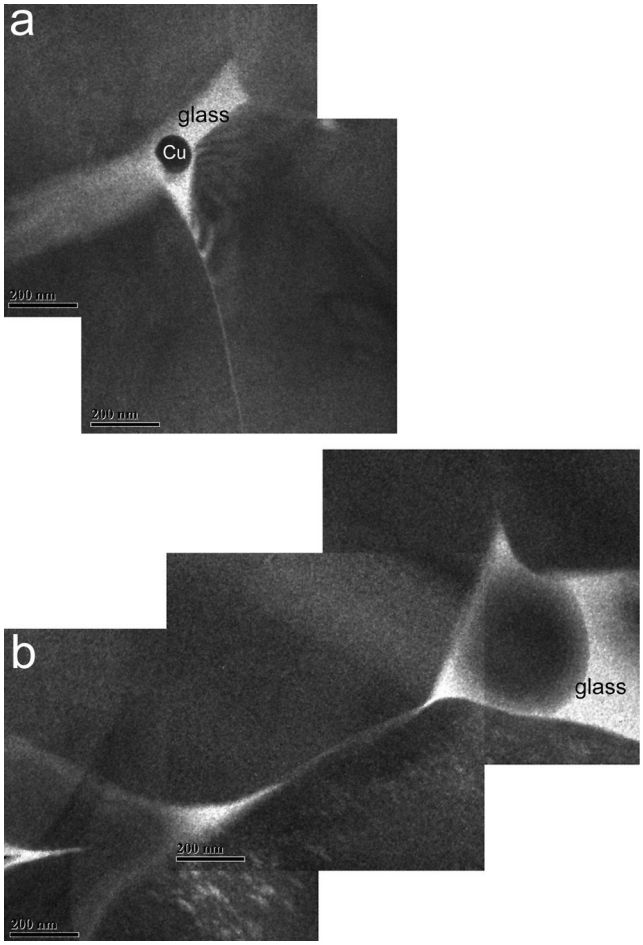

Figure 7. Melt topology of Cu-jacketed sample PL36 (TEM dark-field images). (a) The dark spot in the center of the melt pocket represents exudated copper. (b) Most grain boundaries are wetted by a ~10 nm thick melt film.

$$1\ Ca^{2+} \rightleftharpoons 2\ H^{+},\ \text{from}\ 1\ CaAl_2Si_2O_8 + 1\ H_2O \rightleftharpoons 1\ H_2Al_2Si_2O_8 + 1\ CaO, \quad (6)$$

$$1\ O^{2-} \rightleftharpoons 2(OH)^{-},\ \text{from}\ 1\ CaAl_2Si_2O_8 + 1\ H_2O \rightleftharpoons 1\ CaAl_2Si_2O_7(OH)_2. \quad (7)$$

For reactions (4)–(7) we find creep activation volume and fugacity exponent assuming that strain rate $\dot{\varepsilon}$ is proportional to the defect concentration x. For example, formulating the equilibrium of reaction (4) in terms of Gibb's free energy G^o and activities a of the pure phase components yields

$$0 = \Delta G^o_{(P,T)} + RT \ln \frac{a_{an(4H)} a_{qtz}}{a_{an(Si)} f^4_{H_2O}}. \quad (8)$$

Assuming pure quartz (a_{qtz} = 1), a low hydrogen defect concentration x_{4H}, applying Henry's law ($a_{an(4H)} = x^2_{4H} k^2_{4H}$, two sites per formula unit, where k_{4H} is the Henry constant) and Raoults' law ($a_{an(Si)} = x^2_{an(Si)} \approx 1$), and further assuming no change in reaction entropy and heat capacity, yields

$$0 = \Delta G^o_{P_r} + \Delta V^o (P - P_r) + RT \ln \frac{x^2_{4H} k^2_{4H}}{f^4_{H_2O}}, \quad (9)$$

where ΔV^o is the volume change of solids and P_r a reference pressure of 0.1 MPa. Solving equation (9) for x_{4H} yields the dependence of creep rate on water fugacity and volume change for defect formation

$$\dot{\varepsilon} \sim x_{4H} = k^{-1}_{4H} f^2_{H_2O} \exp\left(-\frac{\Delta G^o + \Delta V^o (P - P_r)}{2RT}\right). \quad (10)$$

This gives a fugacity exponent r = 2 and a formation volume $V_f = \Delta V^o/2$. ΔV^o is not known for formation of hydroanorthite. However, the volume change associated with the replacement of Si^{4+} by $4H^+$ is known for katoite (hydrogrossular), where 3Si in grossular ($Ca_3Al_2(SiO_4)_3$) are replaced by $4H^+$. The resulting volume change is 24 $cm^3\ mol^{-1}$. Since in hydroanorthite only 2Si are exchanged, we assume a volume change of 16 $cm^3\ mol^{-1}$. Adding twice the molar volume of quartz or coesite (~22 $cm^3\ mol^{-1}$, reaction (4)) we obtain $\Delta V^o \approx$ 60 $cm^3\ mol^{-1}$, and $V_f \approx$ 30 $cm^3\ mol^{-1}$. Adding V_f and V = 24 $cm^3\ mol^{-1}$ adopted from dry material yields a total activation volume of V_{4H} = 54 $cm^3\ mol^{-1}$. Estimates of activation volumes and fugacity sensitivities for reactions (4)–(7) are summarized in Table 4. For the reaction 1 $O^{2-} \rightleftharpoons 2\ (OH)^-$ the estimated activation volume is 38 $cm^3\ mol^{-1}$ which agrees with the value of ~36 $cm^3 mol^{-1}$ estimated from the 3-D fitting approach. However, for both estimates the error bar on V may be as large as 20 $cm^3\ mol^{-1}$ due to the implicit assumptions and scatter of the data, respectively.

[33] For wet olivine, *Karato and Jung* [2003] determined V = 24 ± 3 $cm^3\ mol^{-1}$, which is considerably higher than for dry olivine. For wet clinopyroxenite, *Hier-Majumder et al.* [2005] calculated V = 14 ± 6 $cm^3\ mol^{-1}$. In comparison, the activation volume for Si volume diffusion in quartz and olivine is between about −2 to 2 $cm^3\ mol^{-1}$ [*Bejina et al.*, 2003], which is substantially smaller than the values reported above that are estimated from creep tests. It is conceivable that grain boundary diffusion and the formation and migration of jogs and kinks in dislocation creep display higher pressure sensitivity than volume diffusion of point defects.

4.2. Fugacity Sensitivity

[34] From FTIR spectra and TEM observations it is evident that molecular H_2O and water-related point defects

Table 4. Activation Volume and Water Fugacity Dependence of Water-related Defects in Anorthite

Defect[a]	ΔV^o, $cm^3 mol^{-1}$	V, $cm^3 mol^{-1}$	r_{nom}	r_{det}
1 Si^{4+} 4 H^+	60[b]	54	2	1.3 ± 0.4
1 Al^{3+} 3 H^+	38[c]	43	1.5	1.1 ± 0.3
1 Ca^{2+} 2 H^+	17[d]	41	1	1.0 ± 0.3
1 O^{2-} 2 $(OH)^-$	14[e]	38	1	1.0 ± 0.3

[a] ΔV^0 is molar volume of defect formation, V is total activation volume for creep, r_{nom} is predicted water fugacity exponent, r_{det} is fitted fugacity exponent using V.

[b] Estimated from replacement of Si by H in hydrogrossular (see text).

[c] Estimated from molar volume of corundum (~26 $cm^3\ mol^{-1}$) and volume change of ~12 $cm^3\ mol^{-1}$ (assuming ¾ of the volume change for hydrogrossular since only 3 protons are replaced).

[d] Estimated from molar volume of lime (~17 $cm^3\ mol^{-1}$) and formation volume of 0 $cm^3\ mol^{-1}$ since Ca^{2+} ions are much larger than H^+ ions.

[e] Estimated from the average molar volume of minerals that differ by 1 H_2O in composition, e.g., diaspore or boehmite versus corundum (~11 $cm^3\ mol^{-1}$), brucite versus periclase (~13 $cm^3\ mol^{-1}$), portlandite versus lime (~16 $cm^3\ mol^{-1}$) and ice (18 $cm^3\ mol^{-1}$).

Table 5. Flow Law Parameters for Dry and Wet Anorthite Aggregates

Regime[a]	log A, MPa^{-n-r} μm^m s^{-1}	n	Q, kJ mol^{-1}	V, cm^3 mol^{-1}	r	m
Diffusion creep						
Wet	−0.7	1	159	38	1	3
Dry	12.1	1	460	24	0	3
Dislocation creep						
Wet	0.2	3	345	38	1	0
Dry	12.7	3	641	24	0	0

[a] A is a constant, n is stress exponent, Q is activation energy, V is activation volume, r is water fugacity exponent, and m is grain size exponent.

are incorporated in feldspar at elevated confining pressure. Water solubility in anorthite is not well constrained, but FTIR measurements suggest that significant amounts of H_2O are stored in the grain boundary region, and possibly in antiphase domain boundaries. Therefore we assume that both, water content and water fugacity affect the mechanism controlling grain size-sensitive creep of anorthite aggregates at hydrous conditions.

[35] For some silicates like olivine a particular point defect mechanism could be inferred using fugacity sensitivity [*Kohlstedt and Mackwell*, 1998; *Nakamura and Schmalzried*, 1983]. In the feldspar lattice interstitials (Frenkel defects) are more likely to occur than vacancies (Schottky defects) [*Behrens et al.*, 1990]. However, under wet conditions, *Behrens* [1994] suggested that for plagioclase the incorporation of water is linked to vacancies with hydrolysis of Al-O-Si bonds. Simple substitution mechanisms predict water fugacity exponents $r = 1-2$ (Table 4). We refitted the creep data shown in Figure 3 taking into account the activation volume estimated for defect formation under hydrous conditions as discussed above. The resulting fugacity exponents vary between $r = 1.0$ and 1.3 (Table 4) which agrees well to $r \approx 1$ obtained by the 3-D fitting routine. At present, a particular defect mechanism rate-limiting diffusion-controlled creep cannot be determined unequivocally. However, the observed fugacity sensitivity of 1.0 ± 0.3 suggests the replacement of O^{2-} by $2(OH)^-$ (Griggs defect).

[36] The water fugacity sensitivity r of the strain rate was also determined from creep tests on other major silicate rocks. For olivine aggregates, r is in the range of $0.7-1.25 \pm 0.05$ [*Karato and Jung*, 2003; *Mei and Kohlstedt*, 2000a, 2000b] and for clinopyroxenite $r = 1.4 \pm 0.2$ [*Hier-Majumder et al.*, 2005]. For quartz, $r \approx 1$ [*Gleason and Tullis*, 1995; *Hirth et al.*, 2001; *Kohlstedt et al.*, 1995], but values of $r \gtrsim 2$ [*Post et al.*, 1996] and $r = 0.25-0.41$ [*Wang et al.*, 1994] were also reported.

4.3. Effect of Melt Topology in Cu-CuO Buffered Specimens

[37] The samples contained in copper jackets (P136, P137) are about 1 order of magnitude less viscous than specimens buffered in nickel or iron sleeves (Figure 1b and Table 2). We do not expect that the strength of anorthite aggregates depends on oxygen fugacity as no multivalent ionic species are present in the synthetic aggregates. *Wang et al.* [1996] deformed anorthite aggregates from a similar starting material at anhydrous conditions and oxygen fugacities between $f_{O_2} = 10^{-19}-10^{-4}$ MPa and found no effect on strength. However, the Cu-CuO buffered specimens show abundant melt films along grain boundaries that were not observed in other samples (Figure 7). *Dimanov et al.* [2000] report that ~1% melt wetting grain boundaries reduced the

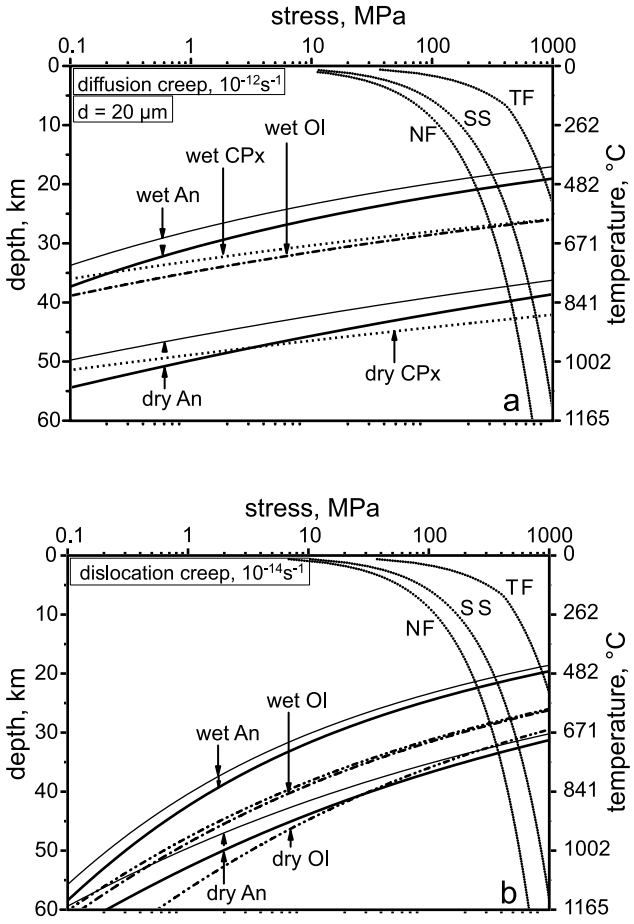

Figure 8. Stress-depth profiles for the continental crust from extrapolated flow laws of synthetic feldspar (An), pyroxene (Cpx), and olivine (Ol) rocks. (a) Grain boundary diffusion creep data are plotted for 20 μm grain size and 10^{-12} s^{-1} strain rate, and (b) dislocation creep data are plotted for a strain rate of 10^{-14} s^{-1}. The extrapolation indicates the effect of activation volume and water fugacity on strength. Thick solid lines are based on flow laws for anorthite aggregates from this study, assuming that the activation volume and water fugacity exponent are similar for diffusion creep and dislocation creep (Table 5). Thin solid lines represent flow laws for anorthite from a previous study [*Rybacki and Dresen*, 2000] that do not include V and r estimates. Short dashed lines represent (Sleaford Bay) clinopyroxenite [*Hier-Majumder et al.*, 2005]. Data for olivine are taken from *Mei and Kohlstedt* [2000a, 2000b] (dash-dotted lines) and *Karato and Jung* [2003] (dash-dot-dotted lines). Temperature calculation corresponds to surface heat flow of 80 mW m^{-2} [*Chapman and Furlong*, 1992]. Fugacities were determined assuming quartz-fayalite-magnetite (QFM)-buffered conditions in the continental crust. NF, SS, and TF denote frictional strength of normal faults, strike-slip faults, and thrust faults, respectively, using Byerlee's law [*Byerlee*, 1978] for a mean crustal density of 2.7 g cm^{-3} and assuming hydrostatic pore pressure.

strength of labradorite aggregates by about 1 order of magnitude compared to specimens where grain boundaries were not wetted. We suggest that the reduced viscosities of the copper-jacketed samples are due to the abundance of melt films along grain boundaries. However, it remains unclear why only the Cu-CuO-buffered samples exhibit melt films. In TEM, metallic Cu was found in glass contained in grain triple junctions (Figures 4d and 7a). It is possible that anorthite and copper form a eutectic with a melting point significantly below that of pure copper ($\sim$1100°C).

4.4. Constitutive Laws and Geological Applications

[38] To determine constitutive equations for high-temperature creep of anorthite aggregates we use the extensive data set of *Rybacki and Dresen* [2000], for which oxygen fugacity was buffered by Fe-FeO, since for all experiments iron jackets were used. For the recalculation of flow law parameters we assume that the activation volume and fugacity sensitivities determined for diffusion creep also hold for dislocation creep. The resulting flow law parameters are given in Table 5, where the water fugacity exponent is set to $r = 1$ and the activation volume is $V = 38$ and 24 $cm^3\ mol^{-1}$ for wet and dry anorthite, respectively.

[39] In extrapolating the data to pressure and temperature conditions relevant for the continental crust we use a strain rate of $10^{-12}\ s^{-1}$ and 20 μm grain size for diffusion-controlled creep (Figure 8a). These may be typical values for localized deformation of ultramylonites in high-temperature shear zones [*Kenkmann and Dresen*, 2002]. For rocks deforming in dislocation creep, data are extrapolated to strain rates of $10^{-14}\ s^{-1}$ (Figure 8b). Stresses predicted from extrapolation of experiments performed at hydrous conditions are less than a factor of 3 higher when the combined effects of activation volume and water fugacity sensitivity are included. However, in extrapolating dislocation creep data of dry anorthite aggregates, stresses increased by about a factor of 10.

[40] In general, feldspar aggregates deformed at hydrous conditions are considerably weaker than dry rocks (Figure 8). For dry rocks the strengths of anorthite and clinopyroxenite deforming in diffusion creep are relatively similar. Similar viscosities are also predicted for anorthite and olivine rocks deforming in dislocation creep. However, at hydrous conditions, feldspar rocks are predicted to be significantly weaker than pyroxenites and olivine rocks (Figure 8). Strikingly, extrapolation of the laboratory data for a given geothermal gradient indicates that fine-grained feldspar and olivine rocks will deform in diffusion creep at lower stresses compared to dislocation creep, suggesting that diffusion creep will dominate in fine-grained ultramylonites.

[41] **Acknowledgments.** We like to thank Michael Naumann for assisting with sample testing, Stefan Gehrmann for preparation of thin sections, Heike Steigert for X-ray analysis, and Reiner Thomas for conducting Raman spectroscopy. Greg Hirth and Shun Karato provided constructive and thoughtful reviews.

References

Behrens, H. (1994), Structural, kinetic and thermodynamic properties of hydrogen in feldspars, paper presented at Processes in Minerals and Ceramics: EFS Workshop on Cation Ordering, Eur. Sci. Found., Cambridge, U.K.

Behrens, H., W. Johannes, and H. Schmalzried (1990), On the mechanisms of cation diffusion processes in ternary feldspars, *Phys. Chem. Miner.*, *17*, 62–78.

Bejina, F., O. Jaoul, and R. C. Liebermann (2003), Diffusion in minerals at high pressure: A review, *Phys. Earth Planet. Inter.*, *139*, 3–20.

Beran, A. (1987), OH groups in nominally anhydrous framework structures: An infrared spectroscopic investigation of Danburite and Labradorite, *Phys. Chem. Miner.*, *14*, 441–445.

Byerlee, J. (1978), Friction of rocks, *Pure Appl. Geophys.*, *116*, 615–626.

Carpenter, M. A. (1991), Mechanism and kinetics of Al-Si ordering in anorthite: I. Incommensurate structure and domain coarsening, *Am. Mineral.*, *76*, 1110–1119.

Chapman, D. S., and K. P. Furlong (1992), Thermal state of the continental lower crust, in *Continental Lower Crust*, edited by D. Fountain, R. Arculus, and R. Kay, pp. 179–199, Elsevier, New York.

Chokshi, A. H., and T. G. Langdon (1991), Overview: Characteristics of creep deformation in ceramics, *Mater. Sci. Technol.*, *7*, 577–584.

Chopra, P. N., and M. S. Paterson (1984), The role of water in the deformation of dunite, *J. Geophys. Res.*, *89*, 7861–7876.

Churakow, S. V., and M. Gottschalk (2003a), Perturbation theory based equation of state for polar molecular fluids: II. Fluid mixtures, *Acta Geochim. Cosmochim.*, *67*, 2415–2425.

Churakow, S. V., and M. Gottschalk (2003b), Perturbation theory based equation of state for polar molecular fluids: I. Pure fluids, *Acta Geochim. Cosmochim.*, *67*, 2397–2414.

Connolly, J. A. D., and B. Cesare (1993), C-O-H-S fluid composition and oxygen fugacity in graphitic metapelites, *J. Metamamorph. Geol.*, *11*, 379–388.

Dimanov, A., G. Dresen, X. Xiao, and R. Wirth (1999), Grain boundary diffusion creep of synthetic Anorthite aggregates: The effect of water, *J. Geophys. Res.*, *104*, 10,483–10,497.

Dimanov, A., R. Wirth, and G. Dresen (2000), The effect of melt distribution on the rheology of plagioclase rocks, *Tectonophysics*, *328*, 307–327.

Dresen, G., Z. Wang, and Q. Bai (1996), Kinetics of grain growth in Anorthite, *Tectonophysics*, *258*, 251–262.

Evans, B., and G. Dresen (1991), Deformation of earth materials: Six easy pieces, *Rev. Geophys.*, *29*, 823–843.

Evans, B., and D. L. Kohlstedt (1995), Rheology of rocks, in *Rock Physics and Phase Relations: A Handbook of Physical Constants*, *Ref. Shelf*, vol. 3, edited by T. J. Ahrens, pp. 148–165, AGU, Washington, D. C.

Freed, A. M., and R. Burgmann (2004), Evidence of power-law flow in the Mojave desert mantle, *Nature*, *430*, 548–551.

Frost, H., and M. Ashby (1982), *Deformation-Mechanism Maps. The Plasticity and Creep of Metals and Ceramics*, Elsevier, New York.

Gleason, G. C., and J. Tullis (1995), A flow law for dislocation creep of quartz aggregates determined with the molten salt cell, *Tectonophysics*, *247*, 1–23.

Gottschalk, M. (1997), Internally consistent thermodynamic data set for rock forming minerals in the system SiO_2–TiO_2–Al_2O_3–Fe_2O_3–CaO-MgO-FeO-K_2O-Na_2O-H_2O-CO_2: An alternative approach, *Eur. J. Mineral.*, *9*, 175–223.

Griggs, D. (1967), Hydrolytic weakening of quartz and other silicates, *Geophys. J. R. Astron. Soc.*, *14*, 19–31.

Griggs, D. T., and J. D. Blacic (1965), Quartz: Anomalous weakness of synthetic crystals, *Science*, *147*, 292–295.

Hetland, E. A., and B. H. Hager (2003), Postseismic relaxation across the Central Nevada Seismic Belt, *J. Geophys. Res.*, *108*(B8), 2394, doi:10.1029/2002JB002257.

Hier-Majumder, S., S. Mei, and D. L. Kohlstedt (2005), Water weakening of clinopyroxenite in diffusion creep, *J. Geophys. Res.*, *110*, B07406, doi:10.1029/2004JB003414.

Hirth, G., C. Teyssier, and W. J. Dunlap (2001), An evaluation of quartzite flow laws based on comparisons between experimentally and naturally deformed rocks, *Int. J. Earth Sci.*, *90*, 77–87.

Hobbs, B. E., A. C. McLaren, and M. S. Paterson (1972), Plasticity of single crystals of synthetic quartz, in *Flow and Fracture of Crust*, *Geophys. Monogr. Ser.*, vol. 16, edited by H. C. Heard et al., pp. 29–53, AGU, Washington, D. C.

Holland, T., and R. Powell (2001), Calculation of phase relations involving haplogranitic melts using an internally consistent thermodynamic dataset, *J. Petrol.*, *42*, 673–683.

Hu, Y., K. Wang, J. He, J. Klotz, and G. Khazaradze (2004), Three-dimensional viscoelastic finite element model for postseismic deformation of the great 1960 Chile earthquake, *J. Geophys. Res.*, *109*, B12403, doi:10.1029/2004JB003163.

Johnson, E. A., and G. R. Rossman (2003), The concentration and speciation of hydrogen in feldspars using FTIR and H MAS NMR spectroscopy, *Am. Mineral.*, *88*, 901–911.

Johnson, E. A., and G. R. Rossman (2004), A survey of hydrous species and concentrations in igneous feldspars, *Am. Mineral.*, *89*, 586–600.

Karato, S. (1981), Pressure dependence of diffusion in ionic solids, *Phys. Earth Planet. Inter.*, *25*, 38–51.

Karato, S., and H. Jung (2003), Effects of pressure on high-temperature dislocation creep of olivine, *Philos. Mag. A*, *83*, 401–414.

Karato, S., and D. C. Rubie (1997), Toward an experimental study of deep mantle rheology: A new multianvil sample assembly for deformation studies under high pressures and temperatures, *J. Geophys. Res.*, *102*, 20,111–20,122.

Karato, S.-I., M. S. Paterson, and J. D. Fitzgerald (1986), Rheology of synthetic olivine aggregates: Influence of grain size and water, *J. Geophys. Res.*, *91*, 8151–8176.

Kenkmann, T., and G. Dresen (2002), Dislocation microstructures and phase distribution in a lower crustal shear zone: An example from the Ivrea-Zone, Italy, *Int. J. Earth Sci.*, *91*, 445–458.

Kenner, S. J. (2004), Rheogical controls on fault loading rates in northern California following the 1906 San Francisco earthquake, *Geophys. Res. Lett.*, *31*, L01606, doi:10.1029/2003GL018903.

Koch, P. S., J. M. Christie, A. Ord, and R. P. George Jr. (1989), Effect of water on the rheology of experimentally deformed quartzite, *J. Geophys. Res.*, *94*, 13,975–13,996.

Kohlstedt, D. L., and S. J. Mackwell (1998), Diffusion of hydrogen and intrinsic point defects in olivine, *Z. Phys. Chem.*, *207*, 147–162.

Kohlstedt, D. L., and Z. Wang (2001), Grain-boundary sliding accommodated dislocation creep in dunite, *Eos Trans. AGU*, *82*(47), Fall Meet. Suppl., Abstract T21C-01.

Kohlstedt, D. L., B. Evans, and S. J. Mackwell (1995), Strength of the lithosphere: Constraints imposed by laboratory experiments, *J. Geophys. Res.*, *100*, 17,587–17,602.

Kronenberg, A. K., and J. Tullis (1984), Flow strength of quartz aggregates: Grain size and pressure effects due to hydrolytic weakening, *J. Geophys. Res.*, *89*, 4281–4297.

Kronenberg, A., S. Kirby, R. Aines, and G. Rossman (1986), Solubility and diffusional uptake of hydrogen in quartz at high water pressures: Implications for hydrolytic weakening, *J. Geophys. Res.*, *91*, 12,723–12,744.

Libowitzky, E., and G. R. Rossman (1997), An IR absorption calibration for water in minerals, *Am. Mineral.*, *82*, 1111–1115.

McDonnell, R. D. (1998), The effect of varying enstatite content on the deformation behavior of wet, fine-grained synthetic peridotite, *Eos Trans. AGU*, *79*(45), Fall Meet. Suppl., F883.

McDonnell, R. D., C. J. Peach, H. L. M. van Roermund, and C. J. Spiers (2000), Effect of varying enstatite content on the deformation behavior of fine-grained synthetic peridotite under wet conditions, *J. Geophys. Res.*, *105*, 13,535–13,553.

Mei, S., and D. L. Kohlstedt (2000a), Influence of water on plastic deformation of olivine aggregates: 1. Diffusion creep regime, *J. Geophys. Res.*, *105*, 21,457–21,469.

Mei, S., and D. L. Kohlstedt (2000b), Influence of water on plastic deformation of olivine aggregates: 2. Dislocation creep regime, *J. Geophys. Res.*, *105*, 21,471–21,481.

Mei, S., S. Majumder, and D. L. Kohlstedt (2001), Influence of water on creep behavior of diopside aggregates, *Eos Trans. AGU*, *82*(47), Fall Meet. Suppl., Abstract T21C-09.

Montesi, L. G. J., and G. Hirth (2003), Grain size evolution and the rheology of ductile shear zones: From laboratory experiments to postseismic creep, *Earth Planet. Sci. Lett.*, *211*, 97–110.

Nakamura, A., and H. Schmalzried (1983), On the nonstoichiometry and point defects of olivine, *Phys. Chem. Miner.*, *10*, 27–37.

Nishimura, T., and W. Thatcher (2003), Rheology of the lithosphere inferred from postseismic uplift following the 1959 Hebgen Lake earthquake, *J. Geophys. Res.*, *108*(B8), 2389, doi:10.1029/2002JB002191.

Ord, A., and B. E. Hobbs (1986), Experimental control of the water-weakening effect in quartz, in *Mineral and Rock Deformation: Laboratory Studies, The Paterson Volume*, *Geophys. Monogr. Ser.*, vol. 36, edited by B. E. Hobbs and H. C. Heard, pp. 51–72, AGU, Washington, D. C.

Paterson, M. S. (1982), The determination of hydroxyl by infrared absorption in quartz, silicate glasses and similar materials, *Bull. Mineral.*, *105*, 20–29.

Paterson, M. S. (1989), The interaction of water with quartz and its influence in dislocation flow: An overview, in *Rheology of Solids and of the Earth*, edited by S. Karato and M. Toriumi, pp. 107–142, Oxford Univ. Press, New York.

Paterson, M. S. (1990), Rock deformation experimentation, in *The Brittle-Ductile Transition in Rocks*, *Geophys. Monogr. Ser.*, vol. 56, edited by A. G. Duba et al., pp. 187–194, AGU, Washington, D. C.

Paterson, M. S., and F. C. Luan (1990), Quartzite rheology under geological conditions, in *Deformation Mechanisms, Rheology and Tectonics*, edited by R. J. Knipe and E. H. Rutter, *Geol. Soc. Spec. Publ.*, *54*, 299–307.

Post, A. D., J. Tullis, and R. A. Yund (1996), Effect of chemical environment on dislocation creep of quartzite, *J. Geophys. Res.*, *101*, 22,143–22,155.

Rutter, E. H., and K. H. Brodie (2004), Experimental intracrystalline plastic flow in hot-pressed synthetic quartzite prepared from Brazilian quartz crystals, *J. Struct. Geol.*, *26*, 259–270.

Rybacki, E., and G. Dresen (2000), Dislocation and diffusion creep of synthetic anorthite aggregates, *J. Geophys. Res.*, *105*, 26,017–26,036.

Rybacki, E., and G. Dresen (2004), Deformation mechanism maps for feldspar rocks, *Tectonophysics*, *382*, 173–187.

Sobolev, S. V., and A. Y. Babeyko (1994), Modeling of mineralogical composition, density and elastic wave velocities in anhydrous magmatic rocks, *Surv. Geophys.*, *15*, 515–544.

Tullis, J., and R. Yund (1980), Hydrolytic weakening of experimentally deformed Westerly Granite and Hale Albite rock, *J. Struct. Geol.*, *2*, 439–451.

Tullis, J., R. Yund, and J. Farver (1996), Deformation-enhanced fluid distribution in feldspar aggregates and implications for ductile shear zones, *Geology*, *24*, 63–66.

Underwood, E. E. (1970), *Quantitative Stereology*, 274 pp., Addison Wesley, Boston, Mass.

Vergnolle, M., F. Pollitz, and E. Calais (2003), Constraints on the viscosity of the continental crust and mantle from GPS measurements and postseismic deformation models in western Mongolia, *J. Geophys. Res.*, *108*(B10), 2502, doi:10.1029/2002JB002374.

Wang, Z.-C., G. Dresen, and R. Wirth (1996), Diffusion creep of fine-grained polycrystalline Anorthite at high temperature, *Geophys. Res. Lett.*, *23*, 3111–3114.

Wang, J. N., B. E. Hobbs, A. Ord, T. Shimamoto, and M. Toriumi (1994), Newtonian dislocation creep in quartzites: Implications for the rheology of the lower crust, *Science*, *263*, 1204–1205.

Wirth, R. (2004), Focused ion beam (FIB): A novel technology for advanced application of micro- and nanoanalysis in geosciences and applied mineralogy, *Eur. J. Mineral.*, *16*, 863–876.

G. Dresen, M. Gottschalk, E. Rybacki, and R. Wirth, GeoForschungsZentrum Potsdam, Potsdam, D-14473, Germany. (uddi@gfz-potsdam.de)